

Highly oriented organic ferroelectric films with single-crystal-level properties from restrained crystallization

Yifan Yuan¹, Yuanyuan Ni¹, Xuanyuan Jiang¹, Yu Yun¹, Jing Li¹, Xiaoshan Xu^{1,2*}

¹*Department of Physics and Astronomy, University of Nebraska, Lincoln, Nebraska 68588, USA*

²*Nebraska Center for Materials and Nanoscience, University of Nebraska, Lincoln, Nebraska 68588, USA*

*xiaoshan.xu@unl.edu

ABSTRACT

Device applications often require thin film growth with quasi-two-dimensional morphology and crystallization which are not always compatible. In this work, we exploit the method of low-temperature deposition followed by restrained crystallization (LDRC) in the growth of crystalline organic molecular thin films, which tend to grow three-dimensionally with random orientations. We demonstrate that, for 2-methylbenzimidazole (MBI), a molecular ferroelectric that tends to crystallize in spherulites, the quasi-two-dimensional films can be grown using LDRC with highly oriented polar axes and single-crystal-level ferroelectric properties. The crystallization process was shown to occur during the post-deposition annealing process using the *in situ* electrical measurements. The limited diffusion, low nucleation density, and low activation energy was found critical for the formation of the plate-shaped quasi-two-dimensional films. These results mark an important step in elucidating the LDRC as an effective and general approach for fabricating films with balanced crystallinity and morphology which are critical for applications.

INTRODUCTION

Thin film growth is crucial for device fabrications, in which quasi-two-dimensional morphology is critical for the application of material properties which also strongly depend on crystallinity. On the other hand, crystallization often conflicts with the ideal morphology because of the complex film/substrate interactions and crystallization dynamics.¹ A way to mitigate the conflict is the low-temperature deposition followed by restrained crystallization (LDRC), in which film deposition and crystallization can be separated and the crystallization can be fine-tuned to optimize functional properties and minimize the impact on morphology. This method has been highlighted recently in fabricating ultra-thin films of hafnia-base ferroelectrics which are promising for integration into modern electronics.²

In this work, we exploit the LDRC method on the growth of organic molecular ferroelectric films, in which both the quasi-two-dimensional morphology and the aligned polar axes are crucial. Organic ferroelectric materials are increasingly important for capacitors, piezoelectrics, and memory devices because they are light weight, flexible, and environment friendly. The last decade has seen the discovery of above-room-temperature ferroelectricity in single-component organic molecular crystals. Their proton-transfer origin of ferroelectricity results in a low coercive field, high remanent polarization, which persist up to the melting temperature (> 400 K). Among them, croconic acid (CA, $C_5H_2O_5$)³ has the highest recorded spontaneous polarization (P_r) of around $30 \mu\text{C}/\text{cm}^2$ and a coercive field (E_c) of about $14 \text{ kV}/\text{cm}$ owing to its hydrogen-bond network which forms a single polar axis^{3,4}. On the other hand, croconic acid films can only be grown in polycrystalline form with randomly oriented polar axes^{5,6}, with a large leakage due to the adhesion of water molecules in air⁷⁻⁹, which hinders the application potential in devices. In contrast, 2-methylbenzimidazole (MBI, $C_8H_8N_2$) is stable in air, has modest acidity¹⁰, and exhibits biaxial polarization¹¹, with P_r of $5.2 \mu\text{C}/\text{cm}^2$ and E_c of $11 \text{ kV}/\text{cm}$. Although fabrication of MBI thin films has been demonstrated by solution shearing¹⁰ and evaporation from solution¹², the former method, which produces plate-like thin films, requires a subtle water affinity of the substrates¹⁰, while the latter method leads to surface roughness comparable to that of the film thickness.

Here, we grow MBI films using low-temperature physical vapor deposition (PVD) in a high vacuum followed by restrained crystallization. Despite the advantages of precise thickness control and minimal contamination¹³, PVD has not been exploited for MBI film growth due to the poor sticking factor, which is related to the low melting temperature (176.5°C in air) that makes the solid phase unstable in high vacuum ($< 10^{-6}$ torr) at room temperature. Hence the low temperatures growth is necessary. The interdigitated Pt electrodes (IDE) on the glass substrates allow in-situ electrical measurements which demonstrate crystallization during the post-growth warming process, resulting in a plate-like morphology with single-crystal-level ferroelectric properties $P_r \approx 2.5 \mu\text{C}/\text{cm}^2$, and coercive voltage $V_c \approx 46.8 \text{ V}$ for in-plane electrodes of $4 \mu\text{m}$ gap. Furthermore, the $[110]$ crystalline direction, which is one of the polar axes, is mostly oriented along the out-of-plane direction. The crystallization process can be understood as a restrained spherulite growth with a low nucleation rate.

RESULTS

- Low-temperature deposition of the amorphous phase

MBI films were deposited at temperature $T_{\text{dep}} = 230$ K on the IDE substrates, while the electrical properties were monitored *in situ* (see the “Methods” section) during the deposition process. All electrical displacement versus applied voltage relations, D - V_{app} , of MBI films are consistent with the linear behavior of capacitors, as shown in Fig. S1a, indicating no ferroelectricity during the low-temperature deposition process. Because the origin of ferroelectricity of MBI is the long-range order of the hydrogen bonds in the crystalline phases^{3,11}, the paraelectric behavior of as-deposited films suggests lack of long-range structural order, likely the amorphous phase; this is expected for low-temperature deposition of MBI whose sublimation temperatures in the high vacuum are around 353 K. The low substrate temperature suppresses the motion of deposited molecules, leaving no sufficient time and kinetic energy for crystallization.

The paraelectric behavior of the amorphous film continues as the thickness of the films increases during the low-temperature deposition. The slope of the D - V_{app} relations for MBI increases (Fig. S1) corresponding to increasing capacitance (Fig. 1a).

The capacitance of the devices in Fig. 1a includes three parts in parallel (see Fig. 1b): C_{glass} from the glass substrate, C_{film} from the film, and C_{vacuum} from the vacuum contribution of the upper half-plane ($C = C_{\text{glass}} + C_{\text{film}} + C_{\text{vacuum}}$). The dielectric constant of the amorphous films can be extracted by separating the contributions. We analyzed the thickness dependence using the partial-capacitance model^{14,15} (Supplementary Note 4). Fitting the thickness dependence of the device capacitance in Fig. 1a, the dielectric constants are found as $\epsilon_{\text{MBI}} = 2.93$, and $\epsilon_{\text{sub}} = 5.63$ for amorphous MBI, and the glass substrates respectively. Notice that ϵ_{MBI} is much smaller than the single-crystal MBI value 33.2 (measured at 1 Hz, 230 K)¹¹, indicating the effect of long-range ferroelectric order in the crystal MBI.

The measured resistance at 200 V is 136 G Ω for the MBI/IDE device with 3.1 μm MBI (230 K, Fig. S1d). The resistance of the as-deposited MBI layer, ≈ 800 G Ω , is much larger than that of the substrate, 154 G Ω , as shown in Fig. 2c and Fig. S2a.

- Crystallization and paraelectric-to-ferroelectric transition in post-deposition annealing.

After the deposition of MBI at 230 K, the films were heated up to 305 K at a 0.2 K/min rate, annealed at 305 K, and later cooled back down to about 260 K. In addition to the D - V_{app} relation, the remanent polarization P_r and capacitance were measured using the double wave method (DWM) (see Supplementary Note 2 and Fig. S6). As the temperature increases, the D - V_{app} relations undergo a transition from the reversible linear behavior to the typical ferroelectric hysteresis loops as shown in Fig. 1c for the 3.1 μm film. To quantify the transition, we plot in Fig. 2a the temperature dependence of P_r which indicates the process of the phase transition.

Since ferroelectricity relies on long-range structural order in the crystalline phase, this transition of P_r , which occurs in a narrow range near 290 K (Fig. 2), corresponds to an amorphous-to-crystalline structural transition, or crystallization from the amorphous phase. According to the definitions of glass transition¹⁶, the crystallization temperature T_x (see Supplementary Fig. S3) for

the MBI film of 3.1 μm is 288.5 K; the corresponding end temperature T_f of the transition (Fig. S3) is 293.2 K.

Above T_f , P_r increases linearly, reaching 2.60 $\mu\text{C}/\text{cm}^2$ at 305 K, with a coercive voltage $V_c \approx 46.8$ V for in-plane electrodes of 4 μm gap measured at 1 Hz. P_r of the MBI films are comparable to the single-crystal values ($P_r \approx 5.2$ $\mu\text{C}/\text{cm}^2$ and $E_c \approx 11$ kV/cm at 300 K, 0.2 Hz)¹¹.

After the substrate temperature reaches 305 K, the film was annealed at 305 K for 7.9 hours. Measurement after the annealing shows a small reduction of P_r (Fig. 2a), which is consistent with the small fraction of film sublimation (with a rate of 5.7 nm/h on average) indicated by the thickness monitor. The temperature dependence of P_r was also plotted in Fig. 2a during the cooling from 305 K to about 260 K at a constant rate of 0.5 K/min. Above T_f , P_r reduces linearly with a slope similar to that during the warming process in the same temperature range, suggesting that this reversible temperature dependence is intrinsic to the ferroelectric MBI crystal. Further cooling through T_x , continues the near-linear reduction of P_r , in contrast to the irreversible phase transition in this temperature range during the warming process. The D - V_{app} loop also becomes more typical for ferroelectric switching due to the reduction of leakage. In most ferroelectrics, P_r decreases with temperature since it is expected to vanish at the ferroelectric-to-paraelectric phase transition temperature. However, for proton-transfer type ferroelectricity that relies on long-range order of hydrogen bonds, like MBI and CA, since the elongation of hydrogen bonds dominates the thermal expansion, a near-linear relationship between strain and ferroelectricity is expected¹⁷, which has also been observed previously in MBI¹⁸ and CA³.

- Transition in electrical capacitance and resistance in post-deposition annealing

The crystallization in the post-deposition annealing is also reflected in the drastic decline in resistance and the sharp increase in capacitance.

The MBI film capacitance was extracted by fitting the non-switching part of the D - V_{app} relation from the DWM measurement and subtracting the substrate capacitance (see Supplementary Note 2 and 3); the results are displayed in Fig. 2b.

Below the phase transition T_x , the dielectric constant of the amorphous film increases slightly with temperature (Fig. 2b) which is common in amorphous materials¹⁹, since thermal excitation promotes the response of the bound charges to the external electric field. During the transition from T_x to T_f , the capacitance increases drastically with temperature due to the much larger dielectric constant of crystalline MBI than that of amorphous MBI. After the completion of the phase transition, while the extracted ϵ_{MBI} is approximately the same as the bulk value (33.2 measured at 1 Hz, 230 K).¹¹

The device resistance (R_{device}) at 200 V and substrate resistance were obtained from I - V_{app} measurements *in situ* with a sweeping rate ≈ 0.55 V/s (≈ 0.7 mHz), in the same annealing process where the D - V_{app} relations were measured. The film resistance (R_{MBI}) and the substrate resistance (R_{sub}) are in parallel, so R_{MBI} were calculated from R_{device} and R_{sub} which was measured before the deposition of films (see Fig. S2).

Below T_x , the I - V curves at low temperature (251.1 K) exhibit linear ohmic behaviors which can be described by a leakage resistance (Fig. 1d). Below 283 K, the glass substrates contribute significantly to the leakage resistance (Fig. S2), although the change of resistance with increasing temperature is dominated by the MBI (Fig. 2c). This is consistent with the small D - V_{app} loop opening up as the temperature increases up to T_x .

Between T_x and T_f , as shown in Fig. 1d, starting around 287.3 K, the polarization-switching peaks appear and become increasingly prominent with increasing temperature, while the linear background also increases with temperature, indicating the reduction of resistance at higher temperatures. The temperature range in which the current peaks are prominent is consistent with that of the amorphous-to-crystal transition. The resistance of MBI undergoes a rapid reduction from 4.43 G Ω at T_x to 1.26 G Ω at T_f (Fig. 2c). This is consistent with the visible leaky behaviors of the D - V_{app} loop at 305 K (Fig. 1c).

Above T_f , most of the amorphous materials have transformed into crystals; the film resistance decreases slowly with increasing temperature.

- Morphology and texture of crystallized MBI films

The morphology of the crystallized films consists of plate-like polycrystalline aggregates, as measured using an *ex situ* laser scanning microscope in ambient conditions. As shown in Fig. 3 and Fig. S7, the plane view of the MBI film shows round-shaped outer envelopes of the aggregates. The height profile (Fig. 3c) can be described as a plateau with a spherical cap on top. The average height is consistent with the nominal thickness of the film, with a small height/diameter aspect ratio of ≈ 0.039 (Fig. 3e), suggesting that the quasi-two-dimensional morphology of the films is mostly kept during the crystallization from the amorphous phase.

A radial alignment of the crystallites within the aggregates can be seen in Fig. 3a. Basically, all the crystallites are of elongated shapes with the longer dimension pointing toward the center of the aggregates. A close-up view of individual crystallites is provided by the atomic force microscopy (AFM) measurements, as shown in Fig. 3b. The crystallites are clearly aligned along their longer dimension. The size of the shorter dimension is about 0.5 μm , as measured from the AFM image in Fig. 3b. This texture of radial alignment is related to the crystal growth mode of spherulites,²⁰ which is often found in polymer films.²¹ Starting with nucleation from the amorphous phase, crystallites grow through the mechanism of small-angle branching, in which numerous needle-like or fibrous crystals spike outward from the nuclei.

The texture of the films can be more precisely described by the crystalline alignment of the crystallites. In spherulites, the radial direction typically corresponds to the crystalline direction of the fastest growth, which has been shown as the c axis of MBI by synchrotron X-ray diffraction measurements previously.¹⁰ The elongated shape of MBI crystallites originates from its anisotropic tetragonal crystal structure¹¹ and the large contrast of surface energy of different crystal planes. As illustrated in Fig. 4a, the MBI molecules, essentially lying flat in the a - b plane of the unit cell, form a chain-like structure via the hydrogen bonds. Between a and b planes, the chains are connected by van der Waals interactions. On the other hand, between different MBI molecular planes, there are much more van der Waals interactions, suggesting larger surface energy of the (001) plane. The growth of crystals tends to minimize the (orientation-dependent) surface energy integrated over the entire crystal.²² Therefore, the fastest growth occurs along the facet direction with the largest surface energy, which for MBI is the [001] direction (c axis), which is the radial direction of the spherulite.

This alignment of the [001] direction along the radial direction of the spherulites is corroborated by the optical images under the cross-polarized microscope (Fig. 4d), where the light passes a linear polarizer, gets reflected by the sample, and passes an analyzer whose axis is perpendicular to that of the polarizer, before finally being captured by the camera. As shown in Fig. 4d, the brightness of the spherulites is minimum when the crystallites are either parallel to the axis of the

polarizer or to that of the analyzer, showing the “Maltese Cross”.²³ MBI crystals, as hinted by the anisotropic crystal structure, are uniaxial birefringent materials with the primary optic axes along the c axis (the radial direction in Fig. 4d) and in the a - b plane. Defining α as the angle between the radial direction of the spherulites and the polarizer axis, if the radial direction corresponds to the c axis, α is also the angle between the c axis and the polarizer axis. As explained in Supplementary Note 5, the amplitude of the light after the analyzer is proportional to $\sin(2\alpha)$, which is consistent with the observation in Fig. 4d.

Besides the alignment of the c axes along the radial directions of the spherulites, the out-of-plane crystalline orientations are also highly aligned, as indicated by the x-ray diffraction measurements. As shown in Fig. 4b, in the $\theta/2\theta$ x-ray diffraction (XRD), which measures the crystal planes parallel to the film plane, (110) and (220) are the two most prominent MBI peaks, indicating that the [110] direction is the dominant out-of-plane direction. The XRD peaks of each film are normalized to the peak intensity of (110) planes. All peaks are indexed by comparing the standard pattern of MBI from CCDC-1199886. High-intensity peaks of MBI are within 50° and the high-angle XRD pattern is shown in Fig. S14.

As illustrated in Fig. 4a, MBI is a bipolar ferroelectric material whose polarization is along the in-plane [110] and $[1\bar{1}0]$ directions, which are also the directions of the molecular chains connected by the hydrogen bonds. Therefore, the two polar axes are either normal to the film surface or in the plane of the MBI films, suggesting that the films can be poled either along the in-plane or along the out-of-plane direction, which is consistent with the successful measurement of switchable polarization using the in-plane electrodes (see Fig. 1).

DISCUSSION

- Limited diffusion and low nucleation density in the restrained crystallization

The crystallization processes of the MBI films studied in this work include nucleation from the amorphous phase followed by the growth of crystallites from the nuclei. When the molecular diffusion is limited, which is the case at low temperature, the growth of the crystallites is restrained along the out-of-plane direction according to the initial quasi-two-dimensional morphology of the amorphous phase. The effect is expected to be more significant for thinner films. Experimentally, as shown in Fig. 4c, the aspect ratio of the plate does increase with thickness, suggesting larger restriction for thinner films, as expected.

Typically, the fast growth of crystallites results in spherulite texture¹ featuring the small-angle branching. Restrained by the quasi-two-dimensional morphology, the spherulites grow into a spherical-cap or plate-like shape. The spherical-cap growth also manifests in the overall crystalline orientation of the films. As the film thickness increases, the peak intensity of the (002) planes gradually increases [see Fig. 4b, c], indicating that the c axes of some crystallites gradually deviate from the film plane in thicker films, consistent with the restrained spherulite growth as schematically illustrated in Fig. 4b inset. In contrast, the deposition of MBI in air at room temperature has no restriction along the out-of-plane direction, resulting in the crystalline phase in the form of three-dimensional spherulites²², with surface roughness similar to the film thickness and without highly oriented crystal structure.

The overall small aspect ratio in Fig. 4c suggests low nucleation density. In this case, each nucleus is expected to grow into crystallites extensively along the in-plane direction while the out-of-plane direction is restrained by the film thickness, forming the plate-shaped morphology.

Experimentally, according to Fig. S12, for the film of thickness $h = 3.1 \mu\text{m}$, the average distance between nuclei is estimated as $48 \mu\text{m}$, which is much larger than the thickness.

Our previous study¹³ on the nucleation kinetics in physical vapor deposition of thin films indicates that the nucleation rate is a non-monotonic function of substrate temperature. At the low-temperature limit, the nucleation rate is low due to the low molecular diffusion; when the temperature is approaching the sublimation (or melting) temperature T_m , the nucleation rate is also low due to the diminishing supersaturation. The maximum nucleation rate occurs at an intermediate temperature as a compromise between diffusion and supersaturation.¹³ For MBI films, the nucleation density and coverage rate decreases rapidly from 216 K to 226 K, while the nucleation density is similar between 226 K and 236 K (Fig. S7). Therefore, the deposition temperature 230 K in 10^{-7} torr pressure for the MBI films in this study is in the high-temperature tail of the nucleation rate-temperature relation, which has the desirable small nucleation rate.

- Low activation energy of the anisothermal amorphous-to-crystalline phase transformation

The formation of spherulites suggests a fast process of crystallite growth, whose origin can be analyzed from the kinetics of the amorphous-to-crystalline transformation.

The kinetics of the amorphous-to-crystalline transformation depends on the characteristics of the nucleation and crystallite growth processes, involving two important parameters, time (t) and temperature (T). Under constant temperature, the kinetics of the transformation can be described by the Johnson-Mehl-Avrami (JMA) equation,²⁴ i.e.,

$$f = 1 - \exp\left[-\left(\frac{t}{\tau}\right)^n\right], \quad (1)$$

where f is the fractional degree to which transformation has taken place by time t , n is the Avrami exponent whose value depends on the characteristics of nucleation and the dimensionality of the crystal growth, τ is the relaxation time satisfying an Arrhenius-type-dependence upon temperature,²⁵ i.e.,

$$\tau = \tau_0 \exp\left(\frac{E}{k_B T}\right), \quad (2)$$

where τ_0 is a temperature-independent pre-exponential factor, E is the activation energy, k_B is the Boltzmann constant. In this work, T varies linearly with time, as described by

$$T = T_0 + kt \quad (3)$$

where T_0 is the initial temperature, $k = 0.2 \text{ K/min}$.

Combining Eq. (1), Eq. (2), and Eq. (3), one has

$$f(T) = 1 - \exp\left[-\left(\frac{T - T_0}{k\tau_0 \exp\left(\frac{E}{k_B T}\right)}\right)^n\right] \quad (4)$$

Although the variation of conductivity or capacitance is often used^{24,26} to measure the fraction of the crystalline phase, for ferroelectric MBI crystals, normalized remanent polarization is used here to measure the degree of phase transformation. Here we subtract the background temperature

dependence of the remanent polarization of the MBI crystal (Fig. 2a) (see Supplementary Note 6), after which the normalized $f(T)$ is plotted in Fig. 5a.

The transformation behavior with the temperature is fitted using Eq. (4) assuming that the Avrami exponent (n) and the activation energy (E) are independent of temperature. The fit parameters are shown in Table 1. To the best of our knowledge, these parameters for MBI haven't been reported before. The activation energy E is the minimum kinetic energy that molecules must acquire to reorganize themselves. Comparing with the activation energy of other materials in Table 2, MBI molecules ($C_8H_8N_2$) have very small activation energy (0.21 eV), which is the origin of the fast crystallite growth of MBI from the amorphous state.

The Avrami exponent n reveals more details on the dimensionality of the crystallite growth. Avrami et. al developed a general equation for transformation kinetics of three-dimensional growth²⁷, $f = 1 - \exp \left[\eta Y_1 Y_2 Y_3 \int_0^t I(t - \tau)^3 d\tau \right]$, where η is a shape factor, Y_i is the anisotropic growth rate, I is the nucleation rate. If the nucleation rate I is constant, this equation leads to Eq. (1) with $n = 4$. In our experiments, the exponent n for MBI is 4.2, indicating that the crystallite growth is three-dimensional and the nucleation rate may increase slightly with temperature.

Typically, initial nucleation occurs preferentially in sites with high interfacial energy or defects, and random nucleation will appear after the saturation of these preferential sites. In terms of crystallization from the amorphous phase, it has previously been suggested that the initial nucleation occurred in the surface layer in amorphous solid water films and the growth front propagated into deep layers,²⁸ due to the higher mobility of molecules in the surface layer than inside the film. Therefore, it is conceivable that MBI's initial nucleation presented in this study may start from the surface layer or the substrate interface shown in Fig. 5b.

CONCLUSIONS

In summary, we show that LDRC is a viable method to fabricate highly-oriented ferroelectric MBI films, where the crystallization is found to occur around 290 K in the post-growth annealing using *in situ* electrical measurements. Besides the restrained crystallization caused by the limited diffusion at low temperature, the plate-shaped quasi-two-dimensional morphology hinges on the low nucleation density, which occurs when the deposition temperature is close enough to the crystallization temperature. The spherulite texture comes from the fast growth of crystallites due to the small activation energy of 0.21 eV. The successful fabrication of the highly oriented quasi-two-dimensional MBI films of single-crystal-level ferroelectric properties marks a breakthrough toward the application of proton-transfer type molecular ferroelectrics. The critical roles of diffusion, nucleation density, and crystallite growth speed revealed in this work will be the important guide for the application of the LDRC method on the growth of other organic molecular films.

METHODS

- Film sample fabrication and electrical measurement

The substrates with interdigitated Pt electrodes on glass were purchased from Metrohm; the electrode width and gap between electrodes are 6 and 4 μm respectively, as shown in Fig. S11b; there are 125 pairs of electrodes of 6760 μm long.²⁹ The physical vapor deposition was performed

in the high vacuum ($< 10^{-6}$ torr) using an EvoVac system (Angstrom Engineering Inc.) equipped with a thickness monitor; the schematic of the system is shown in Fig. 6. The entire deposition and annealing processes are shown schematically in Fig. S13. The deposition was carried out with substrate temperature of 230 K, rate of 1.8 nm/min, for MBI. The temperature of the thickness monitor was kept the same as the substrate during deposition. After the deposition finishes, the substrate is heated at a constant rate of 0.2 K/min in ≈ 3 Torr N_2 environment for MBI. It is confirmed that the change of pressure for MBI has no effect on the hysteresis loops. $D-V_{app}$, DWM, and $I-V_{app}$ loops were measured with Precision RT66C Ferroelectric Tester (Radiant Technologies, Inc.). The frequency was set to 1 Hz to ensure saturated polarization. The electric displacement is calculated as the measured charges divided by the whole electrode area. Before deposition, the $D-V_{app}$ loop for the substrate was measured to ensure no breakdown of electrodes (Fig. S4b). The capacitance during deposition was acquired by fitting the $D-V_{app}$ loops, and the capacitance during annealing from the fitting of leakage polarization in DWM measurements (Fig. S6).

- Morphology and Structural Characterization

X-ray diffraction pattern (XRD) was obtained with the Rigaku Smartlab Diffractometer at room temperature in the atmosphere by θ - 2θ scanning. The samples for XRD measurements are deposited at 230 K on IDE substrate with various thicknesses. The film thickness after deposition was also measured by the DektakXT stylus profiler (Bruker) to calibrate the thickness monitor. Atomic force microscopy (AFM) analysis was performed in the air by using a Bruker Dimension ICON SPM in peak force tapping mode. Optical microscopy (OM) images with height profiles were obtained with Keyence laser scanning microscope VK-X200K. The MBI sample with a thickness of 4.28 μm for OM measurements is deposited at 236 K on the IDE substrate; for AFM measurement the film was deposited at 253 K on the Al_2O_3 substrate.

ASSOCIATED CONTENT

Supporting Information

The Supporting Information is available free of charge at <https://>.

Detailed description of in-situ electrical measurements, capacitance calculation and fitting, the analytical model of IDE sensor, and deposition and annealing process, and supplementary figures (PDF).

Notes

The authors declare that they have no known competing financial interests or personal relationships that could have appeared to influence the work reported in this paper.

ACKNOWLEDGMENTS

This research was primarily supported by the U.S. Department of Energy (DOE), Office of Science, Basic Energy Sciences (BES), under Award No. DE-SC0019173. The research was performed in part in the Nebraska Nanoscale Facility: National Nanotechnology Coordinated Infrastructure and the Nebraska Center for Materials and Nanoscience (and/or NERCF), which are supported by the National Science Foundation under Award ECCS: 1542182, and the Nebraska Research Initiative.

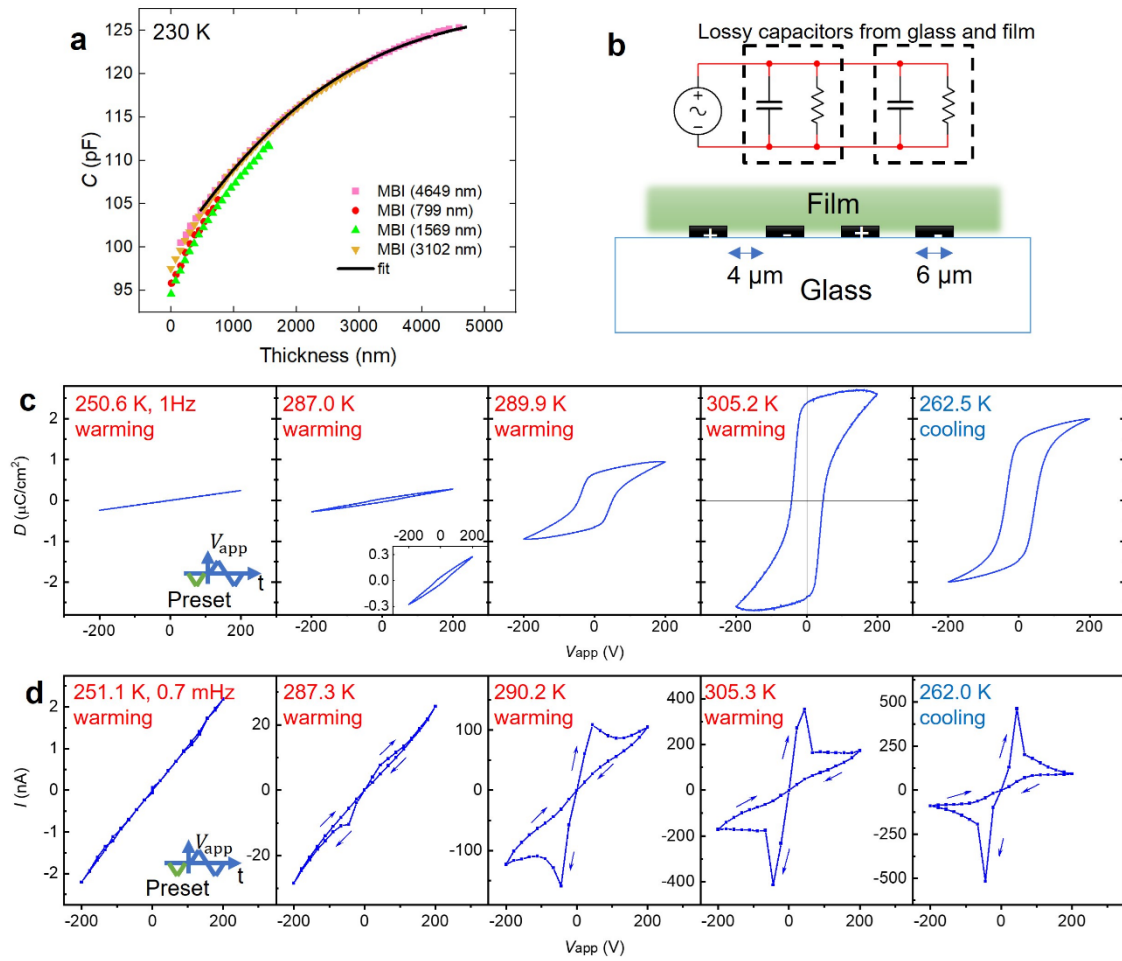


Fig. 1 a) Capacitive response of IDE devices for MBI films with different final thicknesses. The fit was performed with the partial-capacitance model. Note that this model applies for $r > 0.05$ (r is described in Supplementary Note 4). b) Schematic of the IDE device and its equivalent circuit. c) The D - V_{app} loops at 1 Hz, different temperatures corresponding to the red spots in Fig. 2a. The inset in (c) is the close-up view at 287 K. d) The I - V_{app} curves at different temperatures corresponding to the red spots in Fig. 2c. All hysteresis are measured with the same voltage-sweeping protocol shown in the inset.

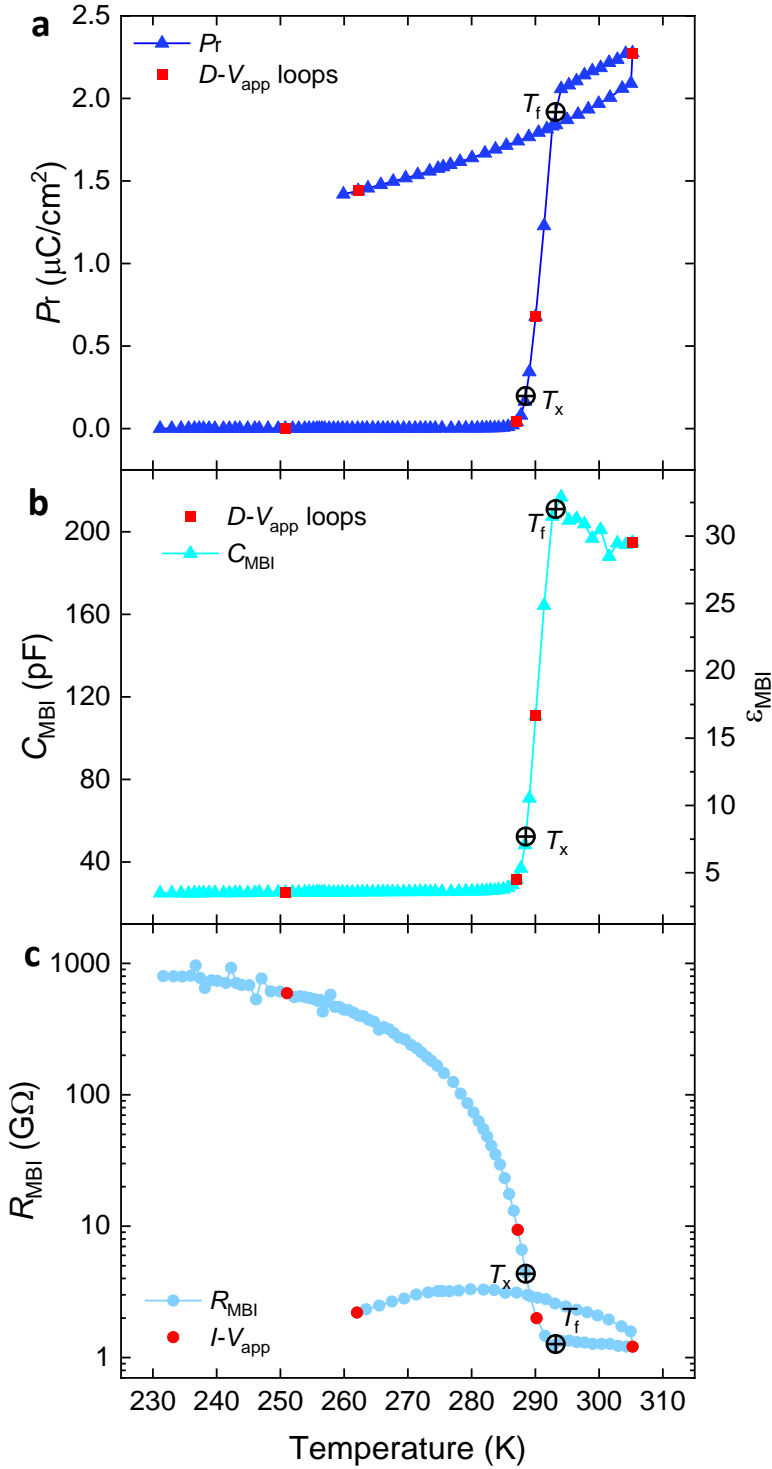


Fig. 2 Crystallization process of MBI manifested in electrical properties during the post-growth annealing. The remanent polarization (a), capacitance (b), and resistance (c) as a function of temperature. The thickness of the sample is 3.1 μm . The resistance is extracted from $I-V_{\text{app}}$ curves at 200 V.

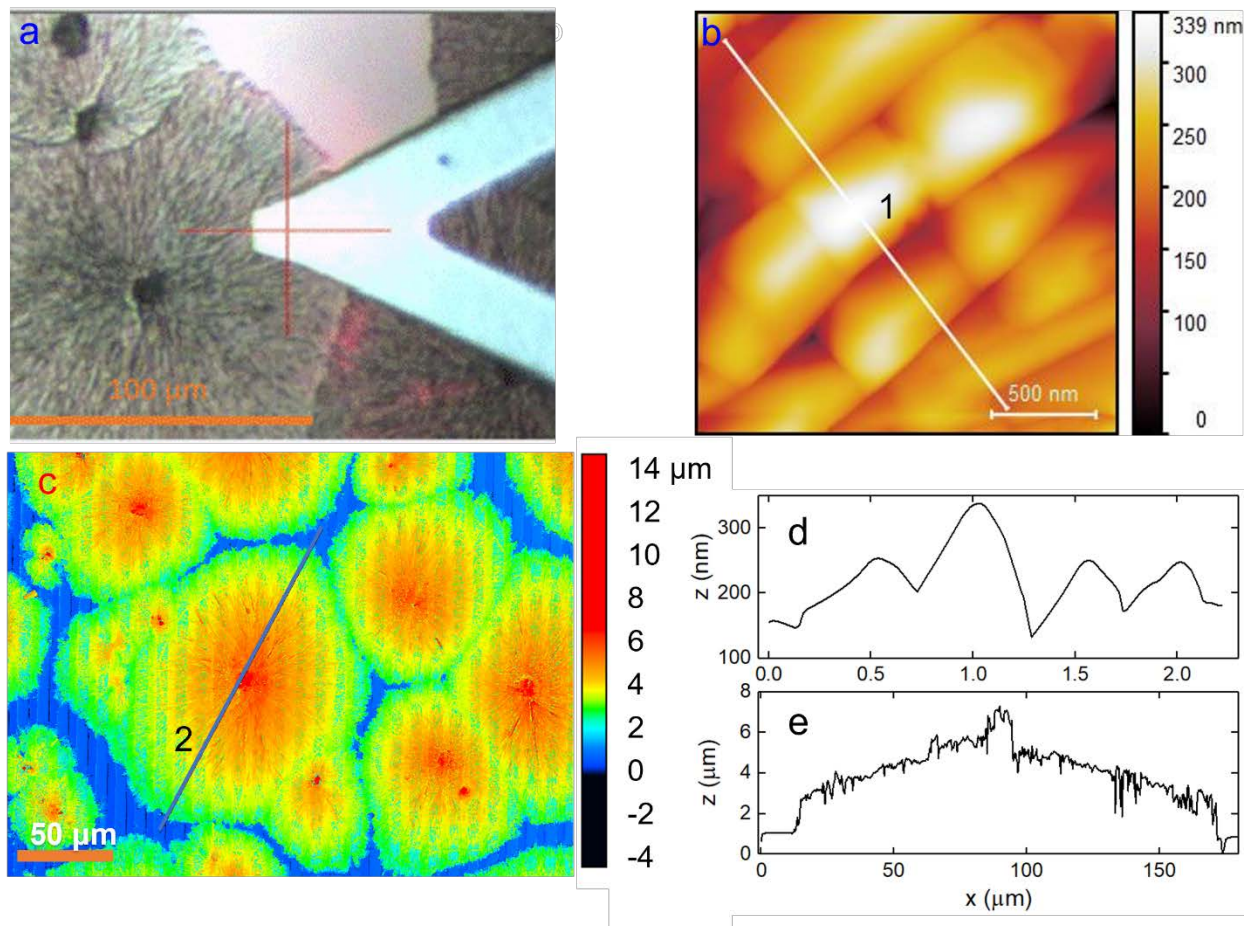


Fig. 3 Morphology of the MBI films. b) AFM image of the assembled spherulite of MBI at the cross position in a). c) Height image of the MBI film with a thickness of 4.28 μm by the laser scanning microscope. In a) MBI crystals deposited on the Al₂O₃ substrate at 253 K. d,e) Height profiles along line 1 in b) and line 2 in c).

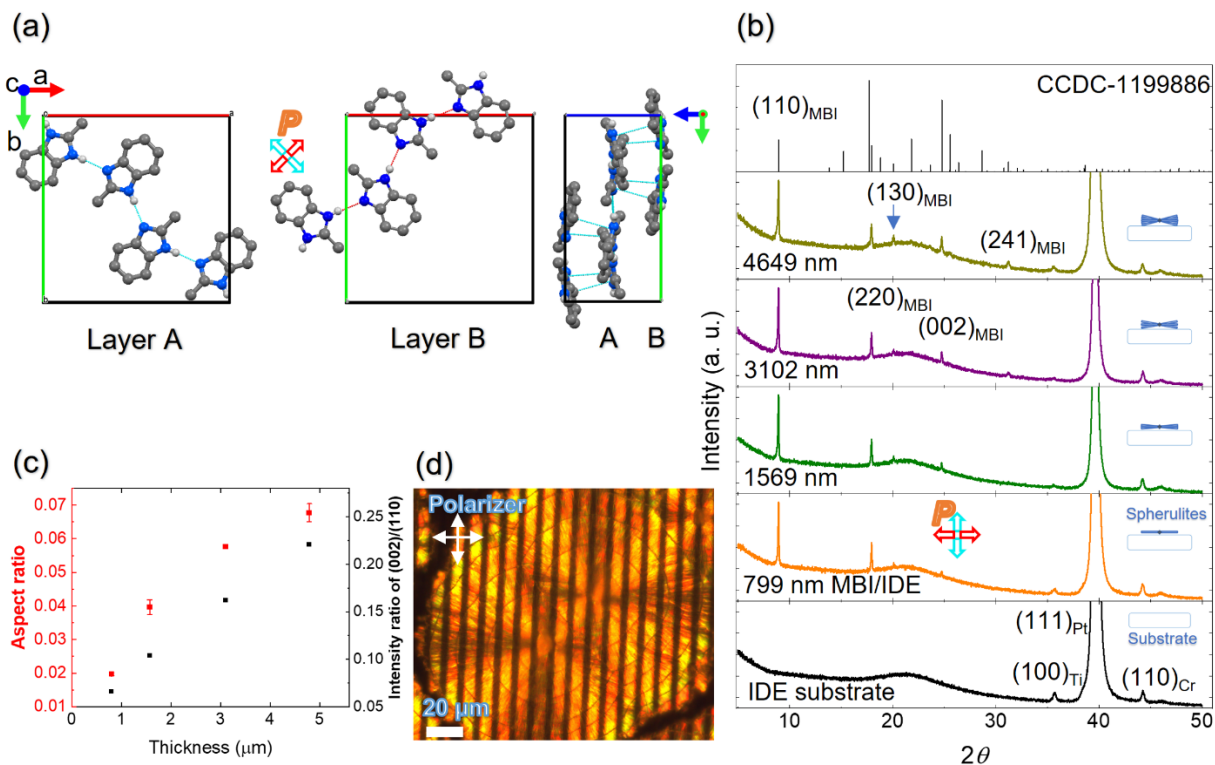


Fig. 4 Texture of the MBI films. a) Schematic illustration of molecular packing and hydrogen bonding in an MBI crystal lattice. Principal polarization axes (hydrogen bonds) run parallel to either $[110]_{\text{tetra}}$ or the crystallographically equivalent $[\bar{1}\bar{1}0]_{\text{tetra}}$ direction. Light blue dash lines represent the short contact with the interatomic distance lower than the sum of van der Waals radii. b) XRD patterns of the MBI films with the out-of-plane diffraction vector for different film thicknesses are compared with the calculated pattern from the MBI powder sample. Small Ti and Cr peaks are from the adhesion layers between Pt and glass. c) The aspect ratio and peak intensity ratio, $(002)/(110)$, as a function of MBI film thickness. The corresponding optical images for different thicknesses are shown in Fig. S12. d) Optical image with crossed polarizers.

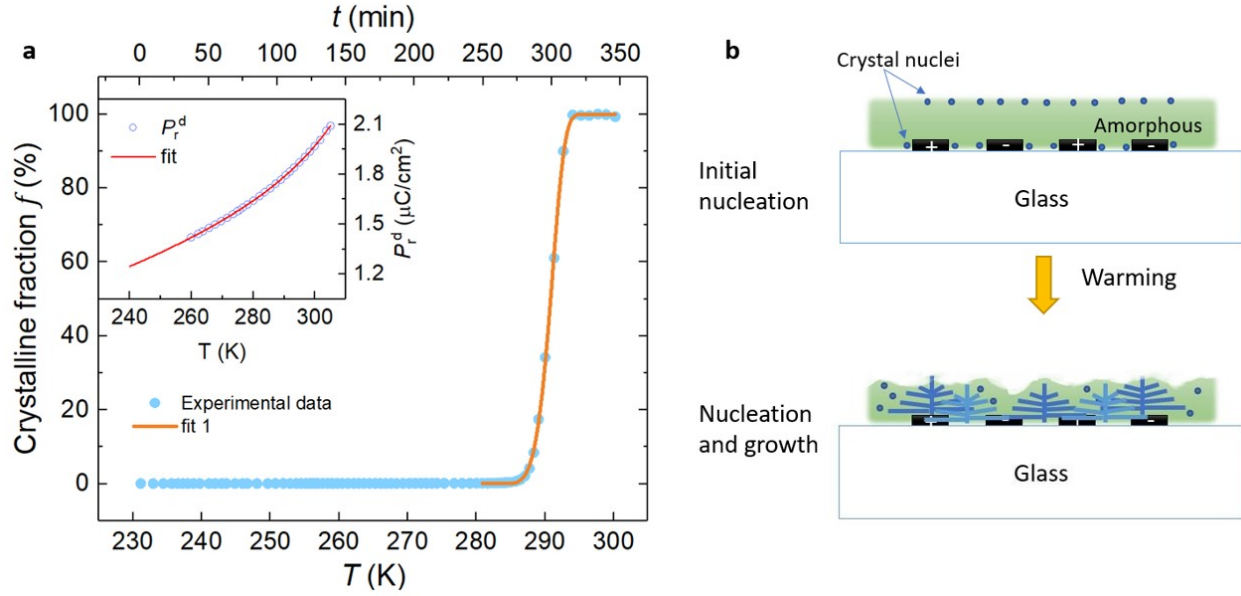


Fig. 5 a) Variation of the crystalline fraction with temperature during annealing. The inset is the variation of remanent polarization with temperature after finishing of phase transition, corresponding to the part in decreasing temperature in Fig. 2(a). The definition of P_r^d and the fit is described in Supplementary Note 6. b) Schematics of the crystal nucleation and growth from amorphous state.

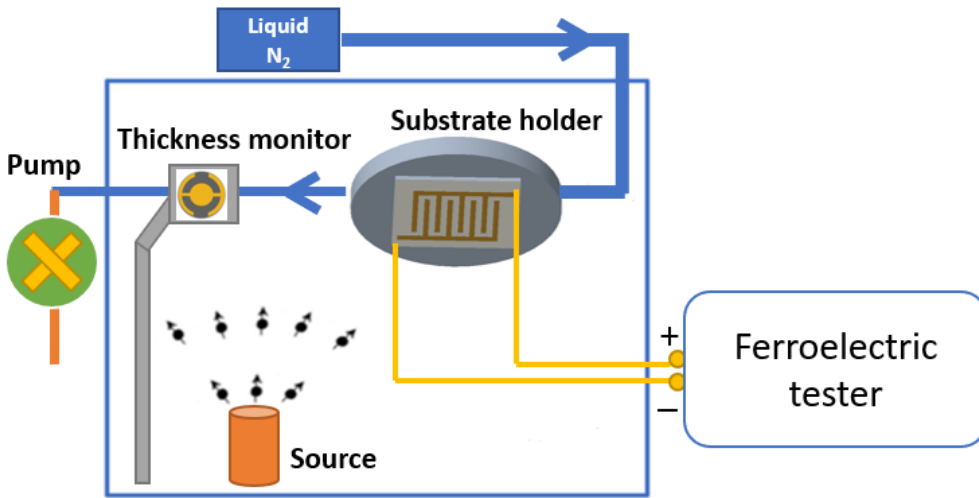


Fig. 6 Schematic of the deposition system with the cooling system.

Table 1 Fitting parameters of Eq. (4) used to describe $f(T)$.				
	E (eV)	n	T_0 (K)	$k\tau_0$ (K)
Fit 1	0.21	4.21	283.4	0.0021

Table 2 Properties of some amorphous materials		
Materials	Crystallization temperature T_x (K)	Activation energy in the amorphous-to-crystalline phase transition (eV)
TaSi ₂ thin films ²⁶	573	1.85
Ge ₂ Sb ₂ Te ₅ films ²⁴	398	3.2
Si films ³⁰	873	3.8
Rubrene ²¹ (C ₄₂ H ₂₈)	323	0.78
MBI	287	0.21

References

- (1) Nishingan, T.; Rudolph, P. *Handbook of Crystal Growth: Basic Techniques and Growth Mechanisms and Dynamics. Bulk Crystal Growth*; Elsevier, 2015.
- (2) Park, M. H.; Lee, Y. H.; Kim, H. J.; Kim, Y. J.; Moon, T.; Kim, K. Do; Müller, J.; Kersch, A.; Schroeder, U.; Mikolajick, T.; Hwang, C. S. Ferroelectricity and Antiferroelectricity of Doped Thin HfO₂-Based Films. *Adv. Mater.* **2015**, *27* (11), 1811–1831. <https://doi.org/10.1002/adma.201404531>.
- (3) Horiuchi, S.; Tokunaga, Y.; Giovannetti, G.; Picozzi, S.; Itoh, H.; Shimano, R.; Kumai, R.; Tokura, Y. Above-Room-Temperature Ferroelectricity in a Single-Component Molecular Crystal. *Nature* **2010**, *463* (7282), 789–792. <https://doi.org/10.1038/nature09363>.
- (4) Horiuchi, S.; Kobayashi, K.; Kumai, R.; Ishibashi, S. Proton Tautomerism for Strong Polarization Switching. *Nat. Commun.* **2017**, *8*. <https://doi.org/10.1038/ncomms14426>.
- (5) Mohapatra, S.; Beaurepaire, E.; Weber, W.; Bowen, M.; Boukari, S.; Da Costa, V. Accessing Nanoscopic Polarization Reversal Processes in an Organic Ferroelectric Thin Film. *Nanoscale* **2021**, *13* (46), 19466–19473.
- (6) Jiang, X.; Lu, H.; Yin, Y.; Zhang, X.; Wang, X.; Yu, L.; Ahmadi, Z.; Costa, P. S.; Dichiara, A. D.; Cheng, X.; Gruverman, A.; Enders, A.; Xu, X. Room Temperature Ferroelectricity in Continuous Croconic Acid Thin Films. *Appl. Phys. Lett.* **2016**, *109* (10). <https://doi.org/10.1063/1.4962278>.
- (7) Ohmi, S.; Takayama, K.; Ishiwara, H. Croconic Acid Thin Film Formation for Ferroelectric Gate OFETs. *MRS Online Proc. Libr.* **2013**, *1587*. <https://doi.org/10.1557/opl.2013.1199>.
- (8) Mohapatra, S.; Da Costa, V.; Avedissian, G.; Arabski, J.; Weber, W.; Bowen, M.; Boukari, S. Robust Ferroelectric Properties of Organic Croconic Acid Films Grown on Spintronically Relevant Substrates. *Mater. Adv.* **2020**, *1* (3), 415–420. <https://doi.org/10.1039/d0ma00147c>.
- (9) Hu, L.; Feng, R.; Wang, J.; Bai, Z.; Jin, W.; Zhang, L.; Nie, Q. M.; Qiu, Z. J.; Tian, P.; Cong, C.; Zheng, L.; Liu, R. Space-Charge-Stabilized Ferroelectric Polarization in Self-Oriented Croconic Acid Films. *Adv. Funct. Mater.* **2018**, *28* (11), 1–9. <https://doi.org/10.1002/adfm.201705463>.
- (10) Noda, Y.; Yamada, T.; Kobayashi, K.; Kumai, R.; Horiuchi, S.; Kagawa, F.; Hasegawa, T. Few-Volt Operation of Printed Organic Ferroelectric Capacitor. *Adv. Mater.* **2015**, *27* (41), 6475–6481. <https://doi.org/10.1002/adma.201502357>.

- (11) Horiuchi, S.; Kagawa, F.; Hatahara, K.; Kobayashi, K.; Kumai, R.; Murakami, Y.; Tokura, Y. Above-Room-Temperature Ferroelectricity and Antiferroelectricity in Benzimidazoles. *Nat. Commun.* **2012**, *3*, 1308. <https://doi.org/10.1038/ncomms2322>.
- (12) Balashova, E. V.; Krichevtsov, B. B.; Svinarev, F. B.; Zaitseva, N. V.; Pankova, G. A. Structural and Dielectric Properties of Organic Ferroelectric 2-Methylbenzimidazole. *J. Surf. Investig. X-ray, Synchrotron Neutron Tech.* **2018**, *12* (2), 233–239. <https://doi.org/10.1134/S1027451018020040>.
- (13) Yuan, Y.; Jiang, X.; Poddar, S.; Xu, X. Electric-Field Assisted Nucleation Processes of Croconic Acid Films. *CrystEngComm* **2019**, *21* (48), 7460–7467. <https://doi.org/10.1039/C9CE01493D>.
- (14) Igreja, R.; Dias, C. J. Analytical Evaluation of the Interdigital Electrodes Capacitance for a Multi-Layered Structure. *Sensors Actuators, A Phys.* **2004**, *112* (2–3), 291–301. <https://doi.org/10.1016/j.sna.2004.01.040>.
- (15) Igreja, R.; Dias, C. J. Dielectric Response of Interdigital Chemocapacitors: The Role of the Sensitive Layer Thickness. *Sensors Actuators, B Chem.* **2006**, *115* (1), 69–78. <https://doi.org/10.1016/j.snb.2005.08.019>.
- (16) Mazurin, O. V. Problems of Compatibility of the Values of Glass Transition Temperatures Published in the World Literature. *Glas. Phys. Chem.* **2007**, *33* (1), 22–36. <https://doi.org/10.1134/S108765960701004X>.
- (17) Mukhopadhyay, S.; Gutmann, M. J.; Jiménez-Ruiz, M.; Jochym, D. B.; Wikfeldt, K. T.; Refson, K.; Fernandez-Alonso, F. Mechanism of Enhancement of Ferroelectricity of Croconic Acid with Temperature. *Phys. Chem. Chem. Phys.* **2017**, *19* (48), 32216–32225. <https://doi.org/10.1039/C7CP06039D>.
- (18) Svinarev, F. B.; Balashova, E. V.; Krichevtsov, B. B. Dielectric Properties of Self-Assembled Spherulite Films of Organic Ferroelectric 2-Methylbenzimidazole. *Ferroelectrics* **2019**, *543* (1), 167–174. <https://doi.org/10.1080/00150193.2019.1592430>.
- (19) Chandel, N.; Imran, M. M. A.; Mehta, N. Comprehensive Studies of Temperature and Frequency Dependent Dielectric and a.c. Conducting Parameters in Third Generation Multi-Component Glasses. *RSC Adv.* **2018**, *8* (45), 25468–25479. <https://doi.org/10.1039/c8ra04214d>.
- (20) Shtukenberg, A. G.; Punin, Y. O.; Gunn, E.; Kahr, B. Spherulites. *Chem. Rev.* **2012**, *112* (3), 1805–1838. <https://doi.org/10.1021/cr200297f>.
- (21) Park, S.-W.; Choi, J.-M.; Lee, K. H.; Yeom, H. W.; Im, S.; Lee, Y. K. Amorphous-to-Crystalline Phase Transformation of Thin Film Rubrene. *J. Phys. Chem. B* **2010**, *114* (17), 5661–5665. <https://doi.org/10.1021/jp910459p>.
- (22) Einstein, T. L. Equilibrium Shape of Crystals. In *Handbook of Crystal Growth*; Elsevier, 2015; Vol. 1, pp 215–264. <https://doi.org/10.1016/B978-0-444-56369-9.00005-8>.
- (23) Hashimoto, K.; Saito, H. Crystallization after Orientation Relaxation in Polypropylene. *Polym. J.* **2008**, *40* (9), 900–904. <https://doi.org/10.1295/polymj.PJ2007187>.
- (24) González-Hernández, J.; Castaño, V.; Del Real, A.; Morales-Sánchez, E.; García-García, E.; Mendoza-Galván, A.; Prokhorov, E. F.; Vorobiev, Y. V. The Mechanism of the Amorphous-to-Crystalline Transition in Ge₂Sb₂Te₅ Ternary Alloys. *Inorg. Mater.* **2000**, *36* (12), 1219–1227. <https://doi.org/10.1023/A:1026677514063>.

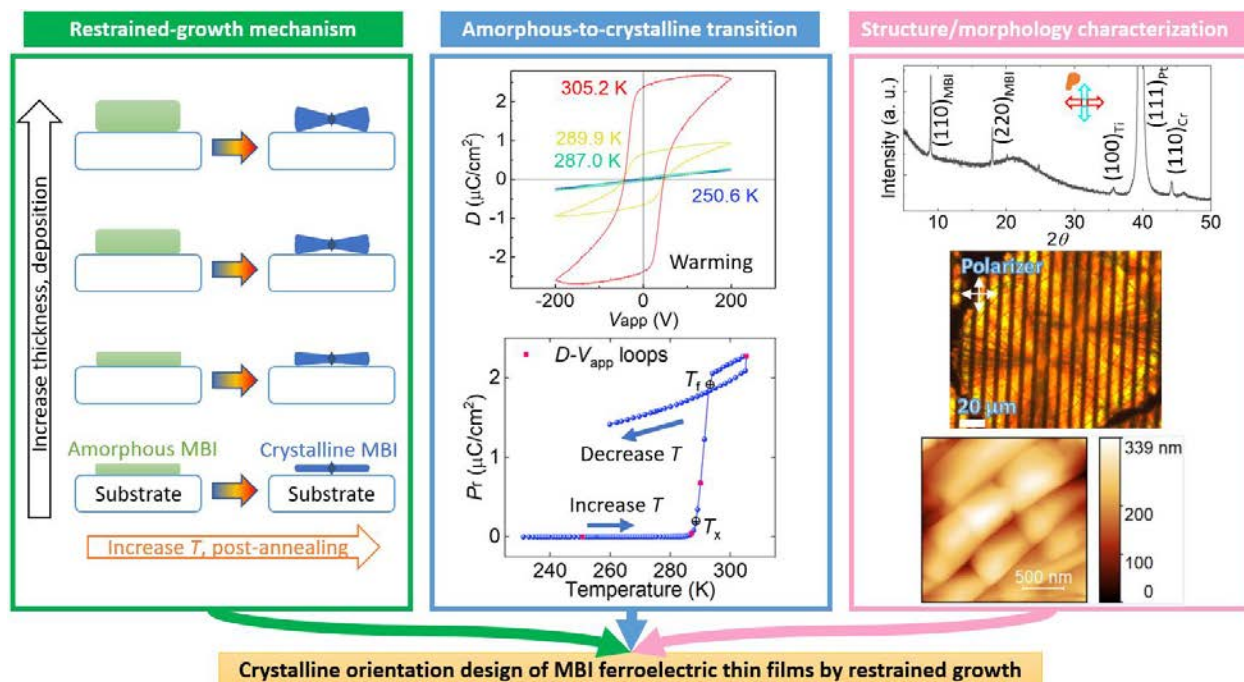
- (25) Markworth, A. J.; Glasser, M. L. Kinetics of Anisothermal Phase Transformations. *J. Appl. Phys.* **1983**, *54* (6), 3502–3508. <https://doi.org/10.1063/1.332416>.
- (26) Tien, T.; Ottaviani, G.; Tu, K. N. Temperature Dependence of Structural and Electrical Properties of Ta-Si Thin Alloy Films. *J. Appl. Phys.* **1983**, *54* (12), 7047–7057. <https://doi.org/10.1063/1.331971>.
- (27) Christian, J. W. *The Theory of Transformations in Metals and Alloys*; International series on materials science and technology; Elsevier Science, 2002.
- (28) Yuan, C.; Smith, R. S.; Kay, B. D. Surface and Bulk Crystallization of Amorphous Solid Water Films: Confirmation of “Top-down” Crystallization. *Surf. Sci.* **2016**, *652*, 350–354. <https://doi.org/10.1016/j.susc.2015.12.037>.
- (29) Yuan, Y. Growth and Characterization of Molecular Ferroelectric Thin Films. Ph.D. Dissertation, University of Nebraska-Lincoln, 2021. <https://www.proquest.com/dissertations-theses/growth-characterization-molecular-ferroelectric/docview/2521534541/se-2?accountid=13360>.
- (30) Lee, J. N.; Lee, B. J.; Moon, D. G.; Ahn, B. T. Effect of Deposition Temperature on the Crystallization Mechanism of Amorphous Silicon Films on Glass. *Jpn. J. Appl. Phys.* **1997**, *36* (Part 1, No. 11), 6862–6866. <https://doi.org/10.1143/JJAP.36.6862>.

For Table of Contents Use Only

Manuscript title: Highly oriented organic ferroelectric films with single-crystal-level properties from restrained crystallization

Authors: Yifan Yuan, Yuanyuan Ni, Xuanyuan Jiang, Yu Yun, Jing Li, Xiaoshan Xu

Table of Contents Graphic



Synopsis

Low-temperature deposition followed by restrained crystallization (LDRC) has been applied to fabricate quasi-two-dimensional films with highly oriented polar axes and single-crystal-level ferroelectric properties of 2-methylbenzimidazole (MBI), a molecular ferroelectric that otherwise tends to crystallize in spherulites. The crystallization process was shown to occur during the post-deposition annealing process using the *in situ* electrical measurements.